

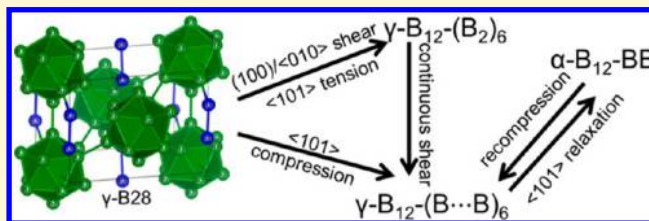
Deformation Induced Solid–Solid Phase Transitions in Gamma Boron

Qi An, William A. Goddard, III,* Hai Xiao, and Tao Cheng

Materials and Process Simulation Center, California Institute of Technology, Pasadena, California 91125, United States

S Supporting Information

ABSTRACT: We predict three new polymorphs of boron by applying density functional theory (PBE flavor) to large shear deformations starting from the recently discovered γ -B₂₈ boron phase (stable above 9 GPa and 1000 K). We find that continuous deformation along the (100)/⟨001⟩ slip system leads to two new phases, named here as γ -B₁₂-(B₂)₆ and γ -B₁₂-(B⋯B)₆. We show that these γ -B₁₂-(B₂)₆ and γ -B₁₂-(B⋯B)₆ phases can also be obtained from uniaxial tensile and compressive deformations of the γ -B₂₈ phase along the ⟨101⟩ direction, respectively. However, the reverse compressive loading on the newly formed γ -B₁₂-(B₂)₆ phase transforms it to itself, not the γ -B₂₈ phase, because of the transferability of the three-center two-electron bond under deformation. This makes the new phase γ -B₁₂-(B₂)₆ a special type of superelastic material. In addition, application of reverse tensile deformation on the newly formed γ -B₁₂-(B⋯B)₆ phase, transforms it to a third new phase, named α -B₁₂-BB, that is metallic, suggesting increased ductility that might make α -B₁₂-BB important for applications in electronic devices. We compared the structural character, mechanical properties, and electronic properties of these new phases to each other and to other phases of boron. We show that the three new phases are dynamically stable at zero pressure. These results show how modifying the connections between boron icosahedra using one to two atom chains can lead to dramatically different mechanical and electronic properties.



1. INTRODUCTION

Elemental boron, located at the borderline of metals and nonmetals in the periodic table, leads to such unique properties as high hardness, high melting temperature, and strong absorbance of neutrons.^{1–5} This makes boron attractive for both scientific research and engineering applications. In particular, boron has the ability of forming three very strong sp² covalent bonds, while leaving available the possibility of different characteristics for forming a fourth bond. In addition, it has the ability of forming an icosahedral shell of boron atoms to stabilize 13 strong multicenter intraicosahedral bonds (Wade's rule). These bonding characteristics lead to an amazing pattern of structures of boron, composed of 12-atom icosahedral clusters connected with each other through a combination of two-center and three-center bonds, leading to at least 16 known polymorphs.⁶

It is important to understand the relationships between all these forms and how the structures control the mechanical and electronic properties. For example, we might stabilize particular forms of boron that exhibit valuable properties by alloying with other elements that fit appropriately into that structure. Such designs require understanding the inter-relationships between the structures and how they can be transformed into each other.

Indeed, the ground state structure for boron is still under debate.⁷ The rhombohedral α -B₁₂ (where B₁₂ clusters are linked at the corners and arranged as cubic close packing) and β -rhombohedral boron structure (where B₁₂ clusters share a common face) have similar energy at ambient conditions, but the disordered β -rhombohedral boron structure becomes more

stable when zero-point vibrational energy or its entropy of partial occupancy is taken into account.^{8,9} Various boron phases were examined experimentally at high temperature and high pressure, on the basis of which a phase diagram was proposed.¹⁰ Recently the equilibrium phase diagram of boron had been constructed on the basis of thermodynamic analysis of experimental and literature data.¹¹ In addition, when the β -rhombohedral boron single crystal is compressed to 100 GPa at room temperature, it is observed to undergo amorphization.³ Moreover, a three-dimensional metallic network with only covalent sp² bonded boron atoms was predicted using first-principles calculations.¹²

Recently, Oganov et al.¹³ used a combination of high pressure synthesis and *ab initio* evolutionary crystal structure search methodology to characterize a new high pressure boron phase, referred to γ -B₂₈. Indeed γ -B₂₈ can be synthesized by compressing the alpha and beta boron phases to 12–20 GPa and heating to 1500–1800 °C. In all cases, γ -B₂₈ remains stable at ambient conditions.¹³ This γ -B₂₈ structure consists of two icosahedra and two B₂ dumbbell pairs (28 atoms) in the unit cell arranging with the space group of *Pnnm*. Several efforts have been made to understand this new phase. For example, the γ -B₂₈ was predicted to be the second hardest elemental material after diamond, with an experimental Vickers hardness of 50–58 GPa.^{14,15} The Vickers hardness of polycrystalline γ -boron was also measured to be 30.3 GPa.¹⁶ Furthermore, the

Received: June 2, 2014

Revised: June 23, 2014

Published: June 24, 2014

structural tension, shearing, and failure processes had been examined via *ab initio* calculations, which found that the two-center boron covalent bonds become less rigid and directional, giving rise to creeping behavior along a particular deformation path of $\langle 011 \rangle$ tension.^{17,18}

Materials respond in many ways to the loading of stress including fracture, plastic deformation, and phase transitions.^{19–21} In particular, Martensitic phase transitions are a hot and widely studied topic.^{22–25} A Martensitic phase transformation is a solid-to-solid phase transition in which the new structure does not require significant atom displacements.^{26,27} It is often observed in materials under high stress, such as the shape memory alloys and Bain transformation between FCC and BCC phases. However, a Martensitic phase transition has never been reported for the pure boron phases although boron has 16 polymorphs. Materials undergoing Martensitic transformations can lead to abrupt changes in the material mechanical, electronic, and transport properties of materials during the phase change. This makes such materials useful for medical sensors, actuators, and energy conversion applications.^{28,29} However, such engineering applications require that the phase transitions proceed without cracking, degradation, or otherwise sustaining damage originating from the stressed transition layer between different phases.³⁰ Unfortunately, most materials exhibiting Martensitic transformations undergo a shape distortion in adjacent grains caused by mismatch stresses, leading to cracking and fracture. For example, polycrystalline ZrO_2 can be strained only to $\sim 2\%$ because of the mismatch stress although its Martensitic phase transitions between tetragonal and monoclinic phases can sustain the shear strain up to 15%.^{22,23} Recent experiments found that the desired superelastic behavior could be achieved through reducing the material scale to nanometers or by arranging the microstructures to be compatible.^{24,25}

In this paper, we applied shear and uniaxial deformations on the recently discovered $\gamma\text{-B}_{28}$ boron using the density functional theory (PBE flavor) calculations. Through deformations of this $\gamma\text{-B}_{28}$ phase, we discovered three new boron phases named $\gamma\text{-B}_{12}\text{-(B}_2)_6$, $\gamma\text{-B}_{12}\text{-(B}\cdots\text{B)}_6$, and $\alpha\text{-B}_{12}\text{-BB}$. In addition, we mapped out the detailed phase transition pathways for these transformations. Our results indicated that the $\gamma\text{-B}_{12}\text{-(B}_2)_6$ phase experiences a transformation to itself under uniaxial deformation. Thus, it could potentially have applications for a special type of superelastic material. We also showed that the phase transformation of $\gamma\text{-B}_{12}\text{-(B}\cdots\text{B)}_6$ to $\alpha\text{-B}_{12}\text{-BB}$ is a nonmetal to metal phase transition that could make it of potential applications to electronic devices. We showed how structures of the three new phases are related to the α -rhombohedral phase and the $\gamma\text{-B}_{28}$ phases. On the basis of these comparisons, we proposed a possible transition pathway from $\alpha\text{-B}_{12}$ phase to $\gamma\text{-B}_{28}$ phase that could provide significance insight into synthesizing both $\gamma\text{-B}_{28}$ and the three new predicted boron phases. We also reported the stability, electronic properties, and mechanical properties of the new phases.

2. METHODOLOGY

2.1. DFT Calculations for Finite Deformations. Here we applied the Perdew–Burke–Ernzerhof (PBE) exchange–correlation functional implemented in the VASP package,^{31–33} while using the projector augmented wave method³⁴ to account for the core–valence interactions. We found that a kinetic energy cutoff of 500 eV for the plane wave expansions gives excellent convergence of the total energies, energy differences, and structural parameters as a function of

deformation. Reciprocal space was sampled using the Γ -centered Monkhorst–Pack scheme with a resolution less than $2\pi \times 1/40 \text{ \AA}^{-1}$. The convergence criteria were set to 1×10^{-6} eV energy difference for solving the electronic wave function and 1×10^{-3} eV/Å force for geometry optimization.

We determined the quasi-static ideal strength by imposing the shear strain, or uniaxial tensile strain, or compressive strain on a particular direction while allowing the structure relaxation along all other five strain components.³⁵ The residual stresses for relaxation of each strain direction is less than 0.5 GPa. For shear deformations of $\gamma\text{-B}_{28}$, we used the unit cell with 28 atoms. To do uniaxial deformation along the $\langle 101 \rangle$ direction, we rotated the unit cell to make cell vector *a* along the $\langle 101 \rangle$ direction, *b* along $\langle 10\bar{1} \rangle$ direction, and *c* along $\langle 010 \rangle$ direction. This rotated cell has total 56 atoms, twice that of the unit cell.

2.2. DFT Calculation on the Properties Prediction. To calculate the phonon modes for the new phases, we used very tight convergence criteria, with 1×10^{-8} eV energy difference and 1×10^{-4} eV/Å force thresholds. Here we calculated the force constants using the supercell approach with finite displacements, as implemented in the PHONOPY code.³⁶

To examine the electronic properties of the three new phases, we also applied the B3PW91 hybrid functional besides PBE functional, which has been established to give an accurate description of band gaps.³⁷ The B3PW91 calculations were conducted using CRYSTAL09 package³⁸ with triple- ζ valence basis sets.³⁹

We computed the elastic moduli from the stress–strain relation as a function of various cell distortions δ from the equilibrium lattice configuration.⁴⁰ The bulk modulus and shear modulus were extracted using the Voigt–Reuss–Hill method⁴¹ from the elastic moduli. Pugh⁴² introduced the ratio between the bulk and shear modulus, B/G , for polycrystalline phases as a measure of fracture/toughness. A high B/G value is associated with ductility brittleness. The Knoop hardness was also computed using the electronegativity approach.^{43,44}

3. RESULT AND DISCUSSION

3.1. Shear Deformation of $\gamma\text{-B}_{28}$ Boron. First we describe the structure and bonding analysis of $\gamma\text{-B}_{28}$ boron. Here we use B_n to represent the unit structures of icosahedra (B_{12}) or interconnecting pairs (B_2), where the subscript *n* indicates the total number of atoms in the unit. Also we use Bn to represent the specific atoms in the crystal structure, where *n* is the atom id. Figure 1a displays the $\gamma\text{-B}_{28}$ boron structure that contains two B_{12} icosahedra and two B_2 pairs in the unit cell. This leads to 36 valence electrons for each B_{12} unit and 6 electrons for each B_2 pair. From PBE calculations, the extra-polyhedral bond lengths for $B3\text{--}B3$, $B2\text{--}B5$, and $B1\text{--}B4$ are 1.66, 1.67 and 1.82 Å, respectively. The extra-pair bond lengths for $B5\text{--}B4$ and $B5\text{--}B1$ are 1.90 and 2.06 Å, respectively. The intra B_2 pair bond ($B5\text{--}B5$) distance is 1.73 Å. All the bond distances of $\gamma\text{-B}_{28}$ boron are summarized in table S1 of Supporting Information (SI).

The bonding in the $\gamma\text{-B}_{28}$ boron can be described as follows. The 10 vertices of each B_{12} unit make connections to the 10 nearby icosahedra through two two-center two-electron (2c-2e) $B3\text{--}B3$ bonds and eight three-center two-electron (3c-2e) $B1\text{--}B5\text{--}B4$ bonds. The remaining two vertices are connected with two B_2 pairs through 2c-2e $B2\text{--}B5$ bonds. Each B_2 pair is connected to two icosahedra through one 2c-2e bond ($B2\text{--}B5$) and to four icosahedra through 3c-2e bonds ($B1\text{--}B5\text{--}B4$). As a result each $B5$ atom contributes half of an electron to the 3c-2e ($B1\text{--}B5\text{--}B4$) bond. Thus, each icosahedron contributes 0.75 electrons to the bond. This indicates that 10 electrons ($4 + 8 \times 3/4$) of the B_{12} unit contribute to the exopolyhedral bonding, while the remaining 26 electrons contribute to intra polyhedral bonding. With $12 + 1 = 13$ intraicosahedral bonds, these B_{12}

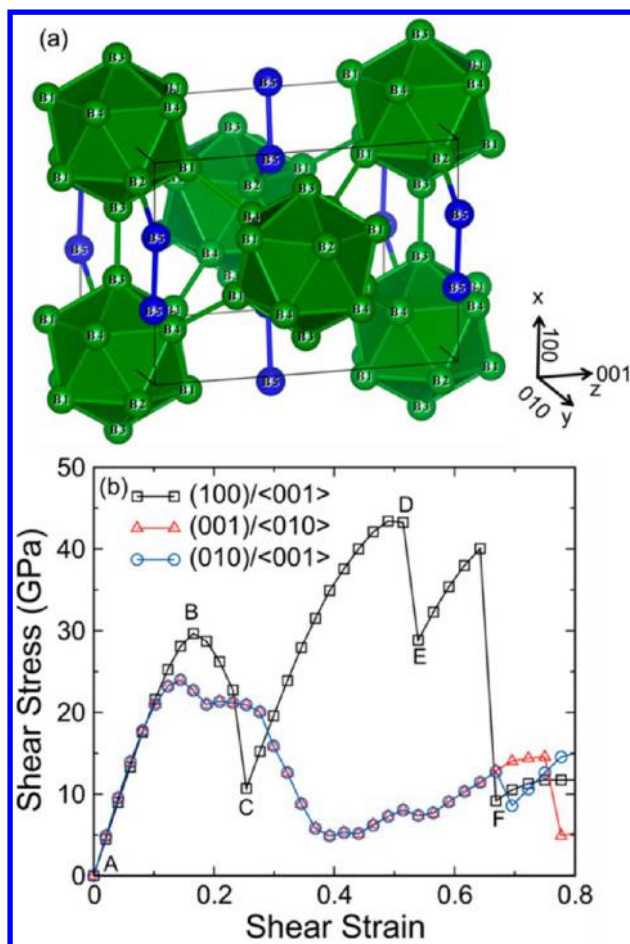


Figure 1. The γ -B₂₈ boron crystal structure and stress–strain curves for shearing along various slip systems: (a) γ -B₂₈ crystal structure: it is constituted by icosahedral B₁₂ clusters (with label B1 through B4) colored in green and dumbbell B₂ pairs colored in blue (with label B5); (b) The stress–strain curves: A corresponds to the γ -B₂₈ boron crystal structure; the two local minimum C and E along (100)/<001> indicate two new phases (γ -B₁₂–(B₂)₆ and γ -B₁₂–(B \cdots B)₆) formed when shearing along (100)/<001>.

units satisfy Wade's $n+1$ skeletal electron pair rule⁴⁵ for maximally stable polyhedral boranes. The electron counts of γ -B₂₈ boron are summarized in table S5 of the SI. This bonding picture of γ -B₂₈ boron is similar to that in the previous study.⁴⁶ To validate this electron-counting scheme, we show the isosurface (at 0.7) of the electron localization function (ELF)^{47,48} in Figure S1 of the SI. The ELF, which ranges from 0 to 1, enables an effective and reliable analysis of covalent bonding. The electron localization can be observed along the long B1–B5 distance of the B1–B4–B5 cluster.

Previous studies^{17,18} had examined the failure modes of the γ -B₂₈ boron under tensile and shear deformations where they considered that it fails when the stress dramatically drops. However, we found that γ -B₂₈ boron undergoes phase transitions, not failure, as the system is sheared along particular slip systems. Thus, we carried out shear simulations to an extended strain of 0.8 for each of three slip systems: (100)/<001>, (001)/<010>, and (010)/<001>. Figure 1b shows the stress–strain relations for the three slip systems. The results indicate that γ -B₂₈ boron undergoes two phase transitions for shearing along the (100)/<001> slip system, but it fails for shear along the other two slip systems. First γ -B₂₈ boron transforms

to a new phase named γ -B₁₂–(B₂)₆ at a strain of 0.254 and then with continuous shearing this γ -B₁₂–(B₂)₆ phase transforms at a strain of 0.539 into a second new phase, named γ -B₁₂–(B \cdots B)₆. We will focus on the structural changes during shearing in this part, and discuss the structural character of new phases in the later section.

To disclose the mechanism of shear-induced phase transitions along (100)/<001> slip system, we plotted selected structures at various strains in Figure 2. We also show the

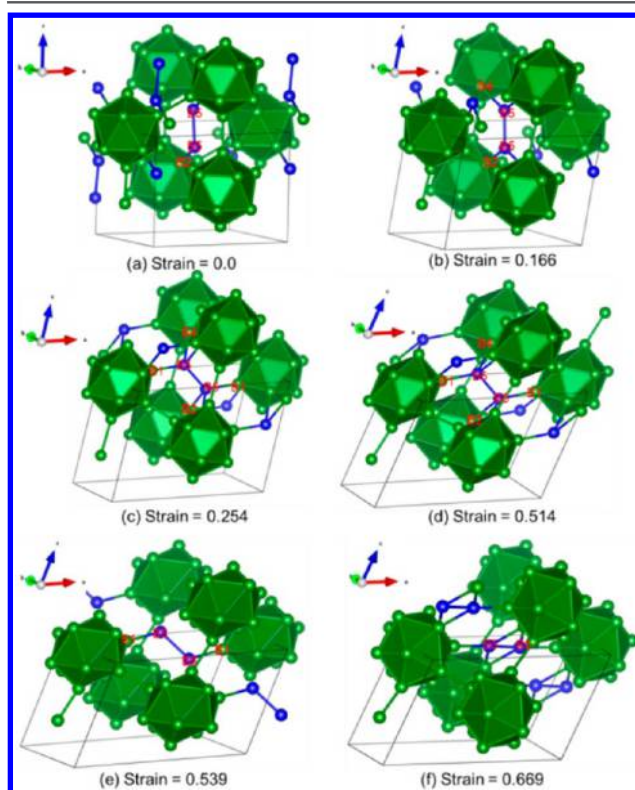


Figure 2. Structural changes as the γ -B₂₈ crystal shears along the (100)/<001> slip system: (a) the intact γ -B₂₈ structure (here the B5–B5 2c-2e bond length = 1.73 Å). (b) The shear stress reaches the first maximum stress before transformation. (c) The γ -B₁₂–(B₂)₆ phase transformed from γ -B₂₈ (here the B5–B5 2c-2e bond length = 1.71 Å). (d) The shear stress reaches the second maximum before the transition to the second phase. (e) The transformed γ -B₁₂–(B \cdots B)₆ crystal structure (here the 3c-2e B5–B5 bond length = 1.79 Å); (f) failure where the B₂ pair is almost parallel to the shear direction. The atoms belonging to the B₁₂ icosahedral clusters and B₂ pairs are represented by green and blue balls, respectively. Here the subfigures correspond to the labels in Figure 1

isosurface (at 0.85) of the ELF in Figure 3. First of all, Figure 2b shows the structure at a strain of 0.166 where the shear stress reaches its first maximum value of 29.7 GPa. The shear shifts the 3c-2e bond (B1–B5–B4) center from the B1–B4 bond to the B4–B5 bond (Figure 3b) by increasing B1–B4 bond from 1.82 to 2.12 Å and decreasing the B4–B5 bond from 1.90 to 1.82 Å. Then continued shear breaks the previous B1–B5–B4 (3c-2e) bond while forming a new B1–B5 (2c-2e) bond with a 1.71 Å bond length and a new B2–B5–B4 (3c-2e) bond at a strain of 0.254 (Figure 3c), leading to the formation of the first new phase, as shown in Figure 2c. The bond lengths for B2–B5, B5–B4, and B2–B4 bonds are 1.83 Å, 1.83 Å, and 1.95 Å, respectively. In this first new phase, γ -B₁₂–(B₂)₆, six vertices of each B₁₂ unit make direct connections to the nearby

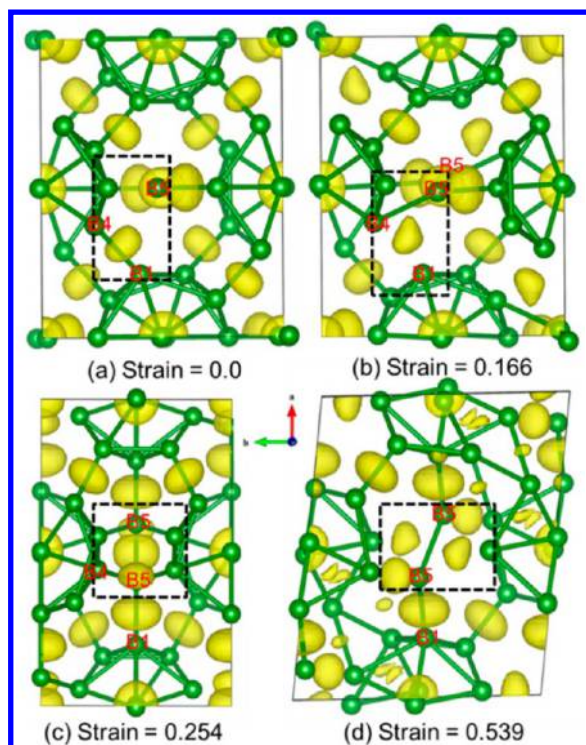


Figure 3. Calculated isosurface of electron localization function during shear (view along $\langle 001 \rangle$ direction) along the $\langle 100 \rangle / \langle 001 \rangle$ slip system: (a) Intact $\gamma\text{-B}_{28}$ structure where the center of the 3c-2e B1–B4–B5 bond is close to the middle of B1–B4 bond. (b) The shear stress reaches the first maximum stress before phase transition where the 3c-2e bond is shifted from B1–B4 to the B4–B5. (c) The transition to $\gamma\text{-B}_{12}-(\text{B}_2)_6$ phase where the B1–B4–B5 bond is broken and a new 2c-2e B1–B5 bond is formed. (d) The transition to $\gamma\text{-B}_{12}-(\text{B}\cdots\text{B})_6$ phase where 2c-2e B5–B5 bond is stretched to 3c-2e bond. The dashed rectangles highlight key regions at which changes occur.

icosahedra, while the other six vertices make connections to B_2 pairs. Thus, each B_2 pair is connected to six icosahedra. Thus, we name this first new phase as $\gamma\text{-B}_{12}-(\text{B}_2)_6$ where the subscript 6 means that each B_2 pair is connected to six icosahedra.

With continued shear on the $\gamma\text{-B}_{12}-(\text{B}_2)_6$ phase, we find that both B2–B5 and B4–B5 stretch to the same bond length of 1.88 Å at the strain of 0.514, at which point the shear stress increases to the second maximum value of 43.4 GPa. Finally at the strain of 0.539, the B2–B5–B4 (3c-2e) bond breaks so that each B_2 pair forms four 3c-2e bonds and two 2c-2e bonds to six nearby icosahedra (Figure 3d). This leads to formation of a second phase as shown in Figure 2e. In this second phase, the bond distance within the B_2 pair is 1.79 Å, appropriate for a 3c-2e bond. Thus, we name the second phase as $\gamma\text{-B}_{12}-(\text{B}\cdots\text{B})_6$ where $\text{B}\cdots\text{B}$ indicates the weak 3c-2e bond. Finally, continued shearing leads to failure at a strain of 0.669 as shown in Figure 2f.

3.2. Tensile Deformation of $\gamma\text{-B}_{28}$ Boron along the $\langle 101 \rangle$ Direction. We showed above that the two new phases are formed by shearing along the $\langle 100 \rangle / \langle 001 \rangle$ slip system. This suggests that the new phases might also be obtained from uniaxial deformation along the $\langle 101 \rangle$ direction. Thus, we did both uniaxial tensile and compressive deformation on $\gamma\text{-B}_{28}$ boron, using positive numbers to represent tensile stress and strain, and negative numbers for compressive conditions.

Figure 4a displays the stress–strain curves under $\langle 101 \rangle$ tension, followed by reverse compression, and then final

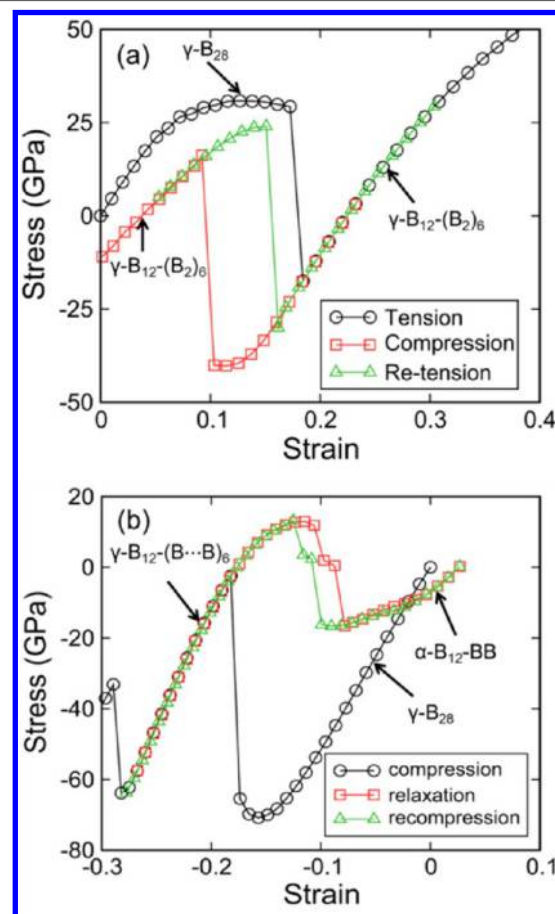


Figure 4. Stress–strain curves for uniaxial deformation of $\gamma\text{-B}_{28}$ crystal along the $\langle 101 \rangle$ direction: (a) The uniaxial tension, reverse compression, and re-tension starting from the $\gamma\text{-B}_{28}$ crystal structure ($\gamma\text{-B}_{28}$ can transform to $\gamma\text{-B}_{12}-(\text{B}_2)_6$ under tension and the new $\gamma\text{-B}_{12}-(\text{B}_2)_6$ can transform to itself (in different orientation) instead of $\gamma\text{-B}_{28}$). (b) The uniaxial compression, reverse tension, and recompression starting from the $\gamma\text{-B}_{28}$ crystal structure ($\gamma\text{-B}_{28}$ can transform to $\gamma\text{-B}_{12}-(\text{B}\cdots\text{B})_6$ phase, a third phase is observed upon relaxation of the $\gamma\text{-B}_{12}-(\text{B}\cdots\text{B})_6$ phase).

retension. To be consistent for these three processes, we used the original cell length of $\gamma\text{-B}_{28}$ boron phase as the reference and calculated the strains along the three deformations. Under the tension process, the stress–strain curve shows that the $\gamma\text{-B}_{28}$ boron undergoes a phase transformation at a strain of 0.184. The relaxation of the transformed structure to zero pressure shows that it is the $\gamma\text{-B}_{12}-(\text{B}_2)_6$ phase. During the second reverse compression process, the phase $\gamma\text{-B}_{12}-(\text{B}_2)_6$ transforms to a new phase at a strain of 0.092. A close examination of the new structure indicates that the new phase is still the $\gamma\text{-B}_{12}-(\text{B}_2)_6$ phase, but with a different crystal orientation. The retension curve in the third process shows that the transformed $\gamma\text{-B}_{12}-(\text{B}_2)_6$ phase will go back to its original structure as it is stretched to a strain of 0.162, indicating that the phase transition to itself is a reversible process.

Figure 5 shows the phase transition path from $\gamma\text{-B}_{28}$ boron to $\gamma\text{-B}_{12}-(\text{B}_2)_6$ phase under tension along $\langle 101 \rangle$ direction. Figure 6 shows the isosurface of ELF for $\gamma\text{-B}_{28}$ boron under $\langle 101 \rangle$ tension and recompression. As $\gamma\text{-B}_{28}$ boron is stretched, it

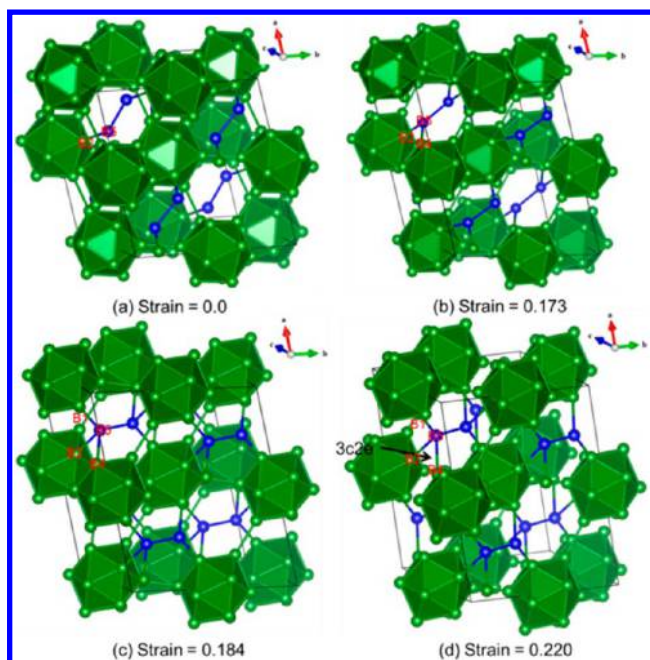


Figure 5. Structural changes for γ -B₂₈ boron under uniaxial tension along $\langle 101 \rangle$ direction. (a) The γ -B₂₈ phase where $\langle 101 \rangle$ along a direction, $\langle 10\bar{1} \rangle$ along b direction, and $\langle 001 \rangle$ along c direction. (b) The tension shrinks the c direction ($\langle 010 \rangle$) and B2–B5–B4 (3c-2e) bond is formed. Now the B5–B5 distance is 1.79 Å. (c) The phase γ -B₁₂–(B₂)₆ is formed where the B5–B2 bond is weakened, leading the formation of B1–B5 bond. (d) Continued tension relaxed the residual stress. The atoms belonging to the B₁₂ icosahedral clusters and B₂ pairs are represented by green- and blue-filled balls, respectively.

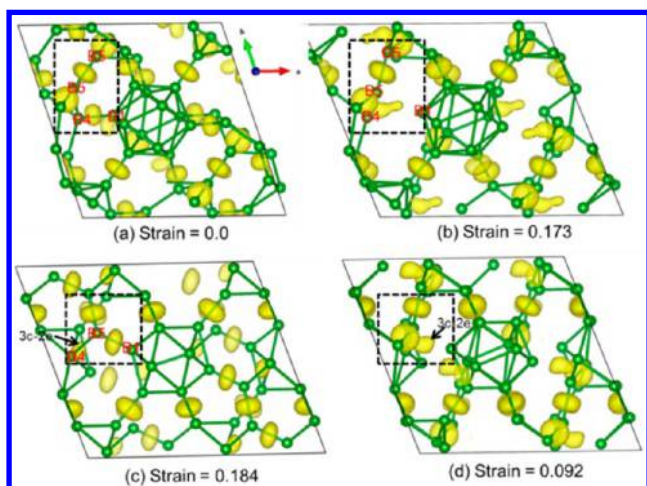


Figure 6. Calculated isosurface of electron localization function for γ -B₂₈ boron under tension and recompression (view along $\langle 010 \rangle$ direction) along the $\langle 101 \rangle$ direction. (a) The intact γ -B₂₈ structure where the center of 3c-2e B1–B4–B5 bond is close to the middle of B1–B4 bond. (b) The tensile stress reach the maximum where the 3c-2e bond center is shifted to B4–B5. (c) The phase γ -B₁₂–(B₂)₆ phase is formed where a new 2c-2e B1–B5 bond and a 3c-2e B2–B4–B5 bond are formed. (d) The recompress leads to the structure transition where the 3c-2e bond is transferred. The dashed rectangles highlight key regions at which changes occur.

contracts along the $\langle 010 \rangle$ direction, so that at a strain of 0.173 the B4–B5 distance decreases from 1.90 to 1.79 Å and the B1–B4 distance increases from 1.82 to 2.56 Å (Figure 5b). This stretching shifts the 3c-2e bond (B1–B5–B4) center from B1–

B4 bond to B4–B5 bond (Figure 6b) similar to the previous shear along $\{100\}/\{001\}$ slip system. Then continued tension increases the B5–B5 bond until at a strain of 0.184, it abruptly shrinks by 13% along the $\langle 010 \rangle$ direction while rotating the B5–B5 bond clockwise (Figure 5c). This leads to formation of a B1–B5 bond with length 1.65 Å, breaking the previous B1–B5–B4 (3c-2e) bond (Figure 6c). Also the B5–B5 bond is decreased to 1.71 Å, and the B2–B5 bond is stretched to 1.79 Å, forming the B2–B5–B4 (3c-2e) bond. Continuous stretching to the strain of 0.22 relaxes the residual stress to nearly zero (Figure 5d).

The structural changes under the reverse compression are shown in Figure 7. The B2–B5–B4 (3c-2e) bond is weakened

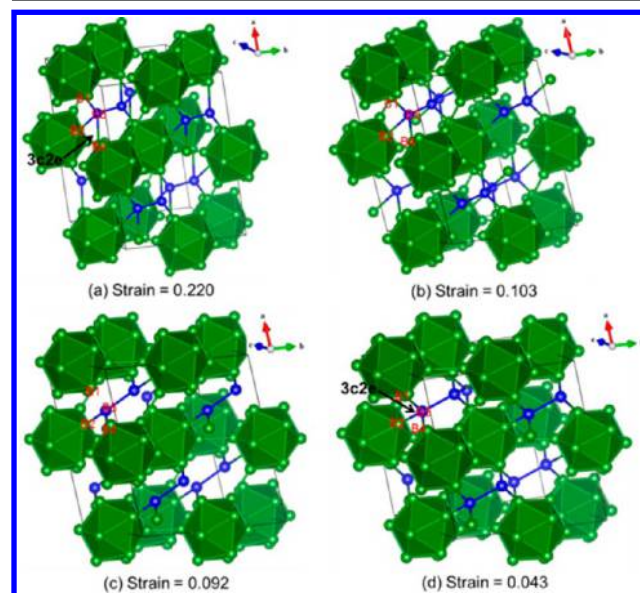


Figure 7. Structural changes of γ -B₁₂–(B₂)₆ transformation to itself under reverse compression. (a) The γ -B₁₂–(B₂)₆ structure at around zero pressure where the 3c-2e bond is B2–B5–B4. (b) The structure before the transformation. (c) The structure after the transformation. (d) The transformed structure at about zero pressure where the 3c-2e bond is changed to B1–B5–B4. The atoms belonging to the B₁₂ icosahedral clusters and B₂ pairs are represented with green and blue balls, respectively.

by compressing both the B2–B5 and B4–B5 bonds to 1.73 Å as the γ -B₁₂–(B₂)₆ phase is compressed to the strain of 0.103 (Figure 7b). This also weakens the B1–B5 bond until it is broken at the strain of 0.092 where the B2–B5–B4 (3c-2e) bond separates into two 2c-2e bonds: B5–B2 and B5–B4 (Figure 7c). As the γ -B₁₂–(B₂)₆ phase is continuously compressed, a new 3c-2e bond B1–B5–B4 forms where the bond length B1–B5 and B4–B5 are 1.83 and 1.81 Å, respectively, leaving two 2c-2e bonds of B2–B5 and B5–B5 with bond lengths 1.69 and 1.74 Å, respectively (Figure 7d and Figure 6d). This leads to a new phase that turns out to be the same γ -B₁₂–(B₂)₆ phase. The above analysis indicates that the transformation of the γ -B₁₂–(B₂)₆ phase into itself arises because of the transferability of 3c-2e bonds under deformation (B2–B5–B4 \leftrightarrow B1–B5–B4). The transformation to itself makes γ -B₁₂–(B₂)₆ a unique type of superelastic material that might possibly avoid the cracking, degradation, and other damage that originates from the mismatch of two phases. Thus, it may have superior properties over other traditional super elastic materials for engineering applications.

3.3. Compressive Deformation of γ -B₂₈ Boron along the $\langle 101 \rangle$ Direction. Figure 4b displays the stress–strain curves under $\langle 101 \rangle$ compression, then reverse tension, and then final recompression. Under compression, the γ -B₂₈ boron transforms to a new phase at a strain of -0.182 while continued compression of the new phase leads to failure at a strain of -0.289 . Here the structure relaxes to zero pressure, indicating that the new phase is γ -B₁₂–(B \cdots B)₆. The ideal compressive strength for γ -B₂₈ boron along $\langle 101 \rangle$ compression is 70.8 GPa at the strain of -0.157 . The subsequent reverse tension curve indicates that the γ -B₁₂–(B \cdots B)₆ phase does not transform back to the γ -B₂₈ phase. Instead it transforms to a third new phase at a strain of -0.087 .

For this third new phase, each icosahedron is connected to six isolated boron atoms and to six icosahedra. This is similar to the boron suboxide (B₆O) and boron carbide (B₁₃C₂) structures.^{49,50} Since boron suboxide can be considered as an oxygen atom inserted into the interstitial positions of α -rhombohedral boron, and boron carbide can be considered as inserting a CBC chain, we name this third phase as α -B₁₂–BB. The final recompression starting from the α -B₁₂–BB phase shows that it transforms back to the γ -B₁₂–(B \cdots B)₆ phase at a strain of -0.131 . Thus, the phase transition between γ -B₁₂–(B \cdots B)₆ and α -B₁₂–BB is reversible.

Figure 8 shows the structural changes under $\langle 101 \rangle$ compression and the subsequent reverse tension. Figure 9

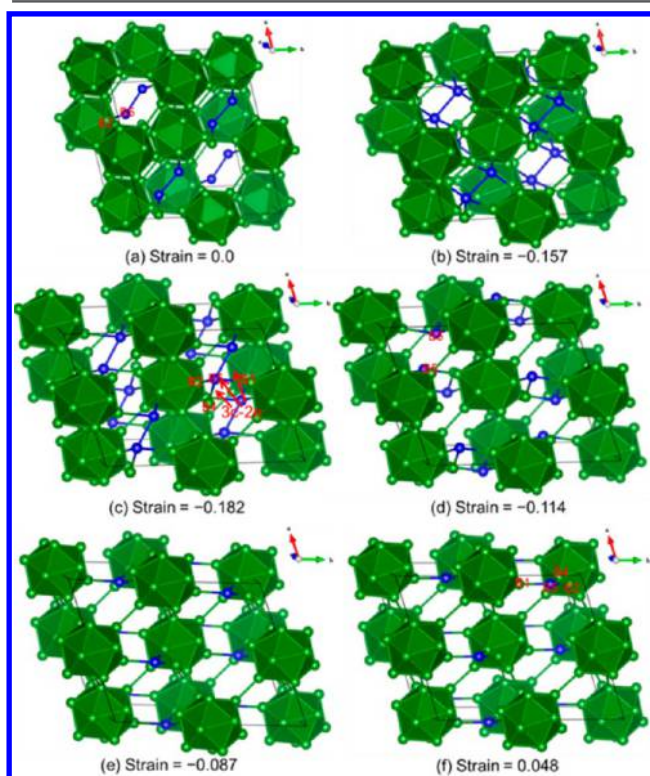


Figure 8. Structural changes for γ -B₂₈ boron under uniaxial $\langle 101 \rangle$ compression, reverse tension. (a) The γ -B₂₈ boron crystal structure. (b) The stress reaches maximum before the phase transition. (c) The γ -B₁₂–(B \cdots B)₆ structure transformed from γ boron. (d) The reverse tension on the γ -B₁₂–(B \cdots B)₆ structure. (e) The α -B₁₂–BB structure transformed from γ -B₁₂–(B \cdots B)₆ structure. (f) Continuous tension relaxed the residual stress. The atoms belonging to the B₁₂ icosahedra and B₂ pairs are represented by green- and blue-filled balls, respectively.

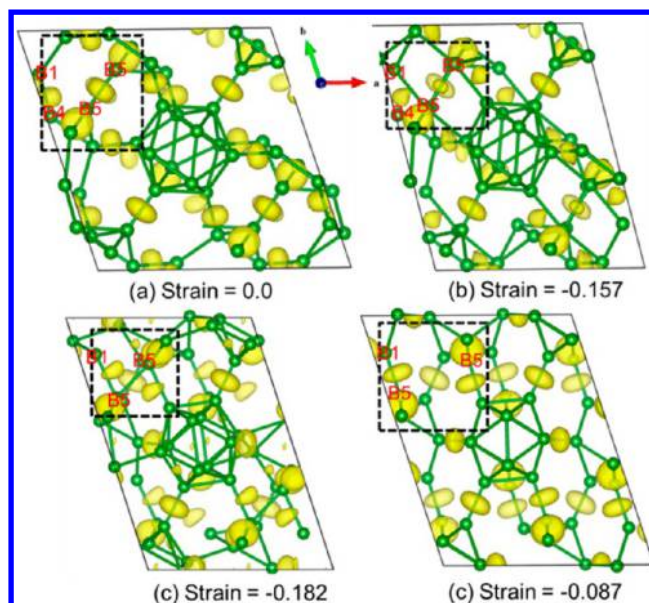


Figure 9. Calculated isosurface of electron localization function for γ -B₂₈ boron under compression and retention (view along $\langle 010 \rangle$ direction) along the $\langle 101 \rangle$ direction. (a) The γ -B₂₈ boron crystal structure where the center of 3c-2e B1–B4–B5 bond is close to the middle of B1–B4 bond. (b) The stress reaches maximum before the phase transition where the 3c-2e bond is shifted to B1–B5, weakening the 2c-2e B5–B5 bond. (c) The γ -B₁₂–(B \cdots B)₆ structure transformed from γ -B₂₈ boron where B5–B5 bond is stretched to form 3c-2e bond. (d) The α -B₁₂–BB structure transformed from γ -B₁₂–(B \cdots B)₆ structure where only 2c-2e bonds exist. The dashed rectangles highlight key regions where changes occur.

shows the isosurface of ELF for γ -B₂₈ boron under $\langle 101 \rangle$ compression and reverse tension. As the γ -B₂₈ phase is compressed to a strain of -0.182 , three new 3c-2e bonds (B1–B5–B4, B4–B5–B4, and B1–B5–B5) are formed in addition to the previously existing B2–B5 bond, leading to formation of the γ -B₁₂–(B \cdots B)₆ phase (Figure 8c and Figure 9c). For the γ -B₁₂–(B \cdots B)₆ phase, six vertices of each B₁₂ unit make connections to nearby icosahedra, while the other six vertices make connections to B₂ pairs. Since the intra B₂ pair bond B5–B5 is 3c-2e bond, which is weaker than a 2c-2e bond, it breaks as the newly formed γ -B₁₂–(B \cdots B)₆ phase is stretched along the $\langle 101 \rangle$ direction to the strain of -0.114 . This tends to form the new α -B₁₂–BB phase at the strain of -0.087 where two isolated B5 atoms are bonded to neighboring B₁₂ icosahedral clusters through three 2c-2e bonds (Figure 8e and Figure 9d).

3.4. Structure and the Bonding Analysis of the New Phase. The structures of three new phases are displayed in Figure 10. The γ -B₁₂–(B₂)₆ phase contains 28 atoms in the unit cell and belongs to the $C2/m$ space group with cell parameters of $a = 8.74$ Å, $b = 4.81$ Å, $c = 7.90$ Å, and $\beta = 141.41^\circ$, resulting in a density of 2.43 g/cm³. Figure 10a shows the unit cell of the γ -B₁₂–(B₂)₆ phase. Each B₁₂ icosahedron is connected to six nearby icosahedra and to six B₂ pairs, while each B₂ pair is connected to six nearby icosahedra. The bond lengths for γ -B₁₂–(B₂)₆ phase are summarized in table S2 of the SI. For each B₁₂ icosahedron, the skeleton bonding contains 26 electrons, satisfying Wade's rule and leaving 10 electrons for extra-polyhedral bonding to neighboring units. Based on the bond distances, eight of the 12 vertices of the B₁₂ icosahedron form 2c-2e bonds to six nearby B₁₂ icosahedra and to two B₂ pairs,

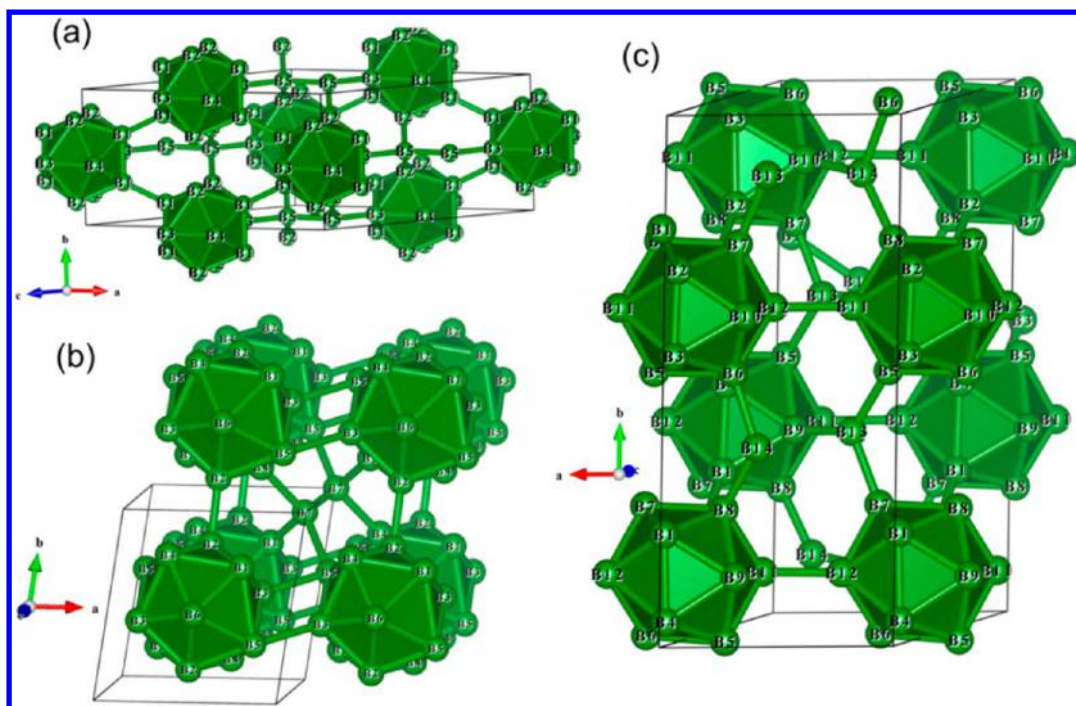


Figure 10. Structures of three new boron phases: (a) the $\gamma\text{-B}_{12}\text{-(B}_2)_6$ phase structure; (b) the $\gamma\text{-B}_{12}\text{-(B}\cdots\text{B)}_6$ phase structure; and (c) the $\alpha\text{-B}_{12}\text{-BB}$ phase structure.

while the remaining four vertices make 3c-2e bonds to the B_2 pairs, requiring $2/3$ electrons ($4 \times 2/3 + 8 = 10$) for each B_{12} icosahedron. Each B_2 pair forms two 2c-2e bonds and two 3c-2e bonds to nearby B_{12} icosahedron, leaving $2/3$ electron to be transferred to the icosahedron. This exactly compensates the $2/3$ electron required for the B_{12} unit, leading to a representation as $\gamma\text{-(B}_{12})^{-2/3}\text{-(B}_2)^{2/3}_6$. The electron counting for the $\gamma\text{-B}_{12}\text{-(B}_2)_6$ phase is summarized in Table S5 of the SI.

Figure 10b shows that the structure of the $\gamma\text{-B}_{12}\text{-(B}\cdots\text{B)}_6$ phase, which contains 14 atoms in the unit cell and belongs to $P\bar{1}$ space group with cell parameters of $a = 4.49 \text{ \AA}$, $b = 4.80 \text{ \AA}$, $c = 5.17 \text{ \AA}$ and $\alpha = 108.19^\circ$, $\beta = 105.61^\circ$, and $\gamma = 80.97^\circ$, resulting in a density of 2.48 g/cm^3 . Similar to the $\gamma\text{-B}_{12}\text{-(B}_2)_6$ phase, each B_{12} icosahedron is connected to six nearby icosahedra and to six B_2 pairs, while each B_2 pair is connected to six nearby icosahedra. The bond lengths for $\gamma\text{-B}_{12}\text{-(B}\cdots\text{B)}_6$ phase are summarized in Table S3 of the SI. For the B_{12} icosahedron, six of the 12 vertices form 2c-2e bonds to four nearby B_{12} icosahedra and two B_2 pairs, and the remaining six make 3c-2e bonds to two nearby B_{12} icosahedra and to four B_2 pairs, saving two electrons ($6 - 6 \times 2/3$) per B_{12} unit. Thus, each B_{12} unit has 26 electrons for intraicosahedral bonding, satisfying Wade's rule. Each B_2 pair forms one 2c-2e bond and three 3c-2e bonds, giving it a neutral charge. The electron counting for the $\gamma\text{-B}_{12}\text{-(B}\cdots\text{B)}_6$ phase is summarized in Table S5 of the SI.

Figure 10c shows the $\alpha\text{-B}_{12}\text{-BB}$ phase, which contains 56 atoms in the unit cell and belongs to the $P21/c$ space group with cell parameters of $a = 5.22 \text{ \AA}$, $b = 11.58 \text{ \AA}$, $c = 8.81 \text{ \AA}$, and $\beta = 119.66^\circ$, resulting in a density of 2.17 g/cm^3 . No B_2 pairs exist in the $\alpha\text{-B}_{12}\text{-BB}$ phase; instead the isolated boron atoms are located between icosahedra. Each B_{12} icosahedron is connected to six nearby icosahedra and to six isolated boron atoms. Each isolated boron atom is connected to three B_{12} icosahedra. The bond lengths for $\alpha\text{-B}_{12}\text{-BB}$ phase are summarized in Table S4 of the SI. For each icosahedron, 12

electrons are utilized in 2c-2e terminal bonding per icosahedron. The isolated boron atom has three 2c-2e bonds. This leaves 24 electrons for intraicosahedral, bonding, makes this phase electron deficient.

3.5. Stability and Transition Path of Boron Phases.

Figure S2 in the SI shows the phonon spectrum of the three new predicted phases where we find no imaginary frequencies in the phonon spectrum, indicating that all three phases are dynamically stable. However, these new phases are thermodynamically less stable than the $\gamma\text{-B}_{28}$ phase (Figure 11). Figure 11 shows the enthalpy difference of these three phases and α -rhombohedral phase as a function of pressure, relative to the $\gamma\text{-B}_{28}$ phase. The $\gamma\text{-B}_{12}\text{-(B}_2)_6$ phase structure can be sustained below 200 GPa, but the discontinuities on enthalpy curves of $\gamma\text{-B}_{12}\text{-(B}\cdots\text{B)}_6$ and $\alpha\text{-B}_{12}\text{-BB}$ phase indicate that these two

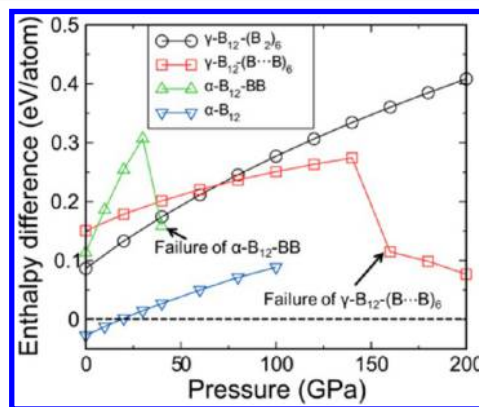


Figure 11. Enthalpy differences of the three new phases and α -rhombohedral boron to the $\gamma\text{-B}_{28}$ phase as a function of pressure. The α -rhombohedral boron has the lowest energy at low pressures until it passes the dashed line where the $\gamma\text{-B}_{28}$ is the ground state structure at high pressures.

phases fail at high pressures, above 40 and 160 GPa, respectively.

It is known that the γ -B₂₈ phase can be synthesized from other boron phases, such as α -rhombohedral boron.¹³ However, the mechanism by which it forms is not known, since B₂ pairs are not present for α -rhombohedral boron. On the basis of the structure character of our new phases and the transition path we examined in the above section, we propose a possible phase transition path from α -rhombohedral boron to the γ -B₂₈ phase. First, inserting an isolated boron atom into the interstitials of boron transforms the α -rhombohedral boron to the α -B₁₂-BB phase. This is similar to the formation of boron suboxide and boron carbide from α -boron.^{49,50} However, the electron deficiency on the new structure makes it distort from the original $R\bar{3}m$ symmetry for α -rhombohedral boron, leading to the space group of $P2_1/c$. The interstitial boron atoms might be achieved experimentally from the defects generated at high temperature. Then compression of the α -B₁₂-BB phase along the $\langle 001 \rangle$ direction brings the two isolated boron atoms together to form the B \cdots B pair, converting α -B₁₂-BB to the γ -B₁₂-(B \cdots B)₆ phase. Additional shearing of the γ -B₁₂-(B \cdots B)₆ phase along $(010)/\langle 10\bar{1} \rangle$ then strengthens the B \cdots B pair to form a σ bond, turning the γ -B₁₂-(B \cdots B)₆ phase to the γ -B₁₂-(B₂)₆ phase. Finally shearing on the γ -B₁₂-(B₂)₆ phase along $(100)/\langle 00\bar{1} \rangle$ will transform the γ -B₁₂-(B₂)₆ to the γ -B₂₈ phase. The relative energy and the transition path are shown in Figure 12.

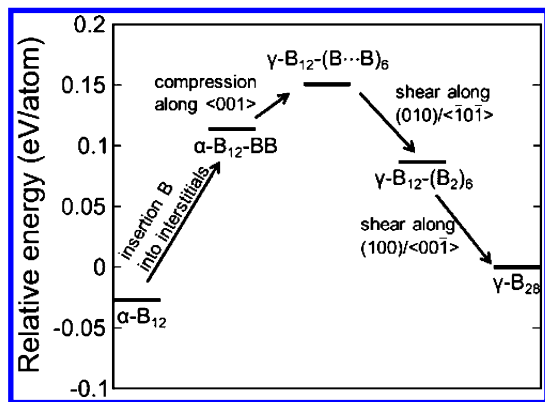


Figure 12. Diagram of α -rhombohedral boron transformation to the γ -B₂₈ boron through the three new metastable boron phases.

3.6. Electronic and Mechanical Properties of the New Boron Phases. It is well-known that the PBE functional grossly underestimates the band gap, while the B3PW91 hybrid functional leads to accurate band gaps.^{37,51,52} Thus, to examine the electronic properties of the new phases, we compute the electronic density of state (DOS) and extract the band gap from both PBE functional and the B3PW91 hybrid functional, which are tabulated in Table 1. We see that the γ -B₁₂-(B₂)₆ and γ -B₁₂-(B \cdots B)₆ phases are semiconducting. But the α -B₁₂-BB phase is metallic. The calculated DOS and band structure for α -B₁₂-BB phase from B3PW91 functional are displayed in Figure 13, while the results for PBE are in Figure S3 in the SI. From the band structures near the Fermi level shown in Figure S4 in the SI, the HOMO goes above the Fermi surface from $\Gamma(0, 0, 0)$ to $Y(0, 1/2, 0)$ in the reciprocal space. Thus, the α -B₁₂-BB phase is metallic because of electron deficiency in the intraicosahedral bonding.

Table 1. Band Gaps for Various Boron Phases Including γ -B₂₈, γ -B₁₂-(B₂)₆, γ -B₁₂-(B \cdots B)₆, and α -B₁₂-BB from PBE and B3PW91 Functional

phases	PBE (eV)	B3PW91 (eV)
γ -B ₁₂ -(B ₂) ₆	0.63	1.83
γ -B ₁₂ -(B \cdots B) ₆	0.08	1.26
α -B ₁₂ -BB	0.0	0.0
γ -B ₂₈	1.45	2.65

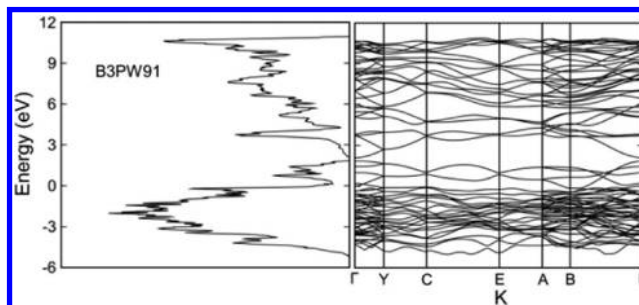


Figure 13. Calculated density of state and band structure of the α -B₁₂-BB phase from B3PW91 functional. (a) The band gap is zero, indicating that this phase is a metallic phase. (b) The HOMO goes above the Fermi surface from $\Gamma(0, 0, 0)$ to $Y(0, 1/2, 0)$ in the reciprocal space, indicating the metallic character.

We also examined the mechanical properties of these new phases by calculating the elastic moduli. The extracted bulk modulus and shear modulus from the elastic moduli are tabulated in Table 2. The elastic moduli for the three new

Table 2. Mechanical Properties for the Three New Phases Including Bulk Modulus (B), Shear Modulus (G), Ductility Index (B/G), and Hardness; the Properties of γ -B₂₈ Phase Are Also Included for Comparison

phases	B (GPa)	G (GPa)	B/G	hardness (GPa)
γ -B ₁₂ -(B ₂) ₆	214.4	179.0	1.19	26.6
γ -B ₁₂ -(B \cdots B) ₆	205.5	201.5	1.02	23.6
α -B ₁₂ -BB	182.7	92.1	1.98	30.6
γ -B ₂₈	223	236	0.95	37.3

phases are listed in Tables S6–S8 of the SI. The B/G values of 1.98 for the α -B₁₂-BB phases suggests (based on Pugh's criteria)⁴² that this phase has the best ductility among all the phases.⁴² Our predicted properties of γ -boron agree very well with previous experiments, especially the ductility index (B/G) of 0.95 compared to the experimental value of 0.94.¹⁶ The calculated hardness of the new phases are listed in Table 2. Although the three new phases are less hard than the original γ -B₂₈ phase, their high hardness indicates that these three new phases could be the basis for alloying to achieve hard ductile materials. The α -B₁₂-BB has the largest hardness (30.6 GPa) among the new phases.

4. CONCLUSIONS

In summary, we predicted three new boron phases through deformations of γ -B₂₈ boron. The γ -B₁₂-(B₂)₆ phase experiences a superelastic transformation into itself under uniaxial deformation because of the transferability of 3c-2e bonds under deformation. This super elastic property might make it useful for switching applications in medical sensors and energy conversions.

The γ -B₁₂-(B₂)₆ and γ -B₁₂-(B··B)₆ phases are nonmetals at zero pressure, while the α -B₁₂-BB phase is metallic. Thus, the phase transition of γ -B₁₂-(B··B)₆ to α -B₁₂-BB is a nonmetal to metal phase transition, that might lead to engineering applications in electronic devices.

Some key points of these simulations are

- Continuous shearing the γ -B₂₈ boron along the $\langle 100 \rangle / \langle 001 \rangle$ slip system leads to the γ -B₂₈ to γ -B₁₂-(B₂)₆ phase transition, and γ -B₁₂-(B₂)₆ to γ -B₁₂-(B··B)₆ phase transition, respectively.
- Tensile deformation of γ -B₂₈ boron along the $\langle 101 \rangle$ direction leads to the phase transition from γ -B₂₈ to γ -B₁₂-(B₂)₆. The reverse compressive deformation of the γ -B₁₂-(B₂)₆ phase leads to a transformation to itself. This transformation is a reversible process.
- Compressive deformation of γ -boron along $\langle 101 \rangle$ direction leads to the phase transition from γ -B₂₈ to γ -B₁₂-(B··B)₆. The reverse tensile deformation of the γ -B₁₂-(B··B)₆ phase leads to a transformation to α -B₁₂-BB. This γ -B₁₂-(B··B)₆ to α -B₁₂-BB phase transformation is a reversible process and a nonmetal to metal phase transition.

■ ASSOCIATED CONTENT

■ Supporting Information

The SI includes the tables of interatomic distance of γ -B₂₈ boron, interatomic distance of γ -B₁₂-(B₂)₆ boron, interatomic distance of γ -B₁₂-(B··B)₆ boron, interatomic distance of α -B₁₂-BB boron, the electron counts for the boron phases of γ -B₂₈, γ -B₁₂-(B₂)₆, γ -B₁₂-(B··B)₆, and α -B₁₂-BB, the predicted elastic moduli for γ -B₁₂-(B₂)₆ boron, γ -B₁₂-(B··B)₆, and α -B₁₂-BB boron. It also include the figures of the isosurface of ELF for γ -B₂₈ boron, the phonon spectrum of three new boron phases, the density of state and band structure of the α -B₁₂-BB phase from PBE hybrid functional, and the band structures of α -B₁₂-BB phase near the Fermi surface calculated from PBE functional. It also includes the cif files for the metastable phases of γ -B₁₂-(B₂)₆, γ -B₁₂-(B··B)₆, and α -B₁₂-BB. This material is available free of charge via the Internet at <http://pubs.acs.org>.

■ AUTHOR INFORMATION

Corresponding Author

*wag@wag.caltech.edu

Notes

The authors declare no competing financial interest.

■ ACKNOWLEDGMENTS

This work was supported by the Defense Advanced Research Projects Agency (W31P4Q-13-1-0010, program manager, Judah Goldwasser). In addition some support was provided by the Army Research Laboratory under Cooperative Agreement Number W911NF-12-2-0022. The views and conclusions contained in this document are those of the authors and should not be interpreted as representing the official policies, either expressed or implied, of the Army Research Laboratory or the U.S. Government. The U.S. Government is authorized to reproduce and distribute reprints for Government purposes notwithstanding any copyright notation herein. We thank Dr. Sergey V. Zybun for the useful discussions.

■ REFERENCES

- (1) Young, D. A. *Phase Diagrams of the Elements*; University of California Press: Berkeley, CA, 1991.
- (2) Zarechnaya, E.; Dubrovinskaya, N.; Caracas, R.; Merlini, M.; Hanfland, M.; Filinchuk, Y.; Chernyshov, D.; Dmitriev, V.; Dubrovinsky, L. *Phys. Rev. B* **2010**, *82*, 184111.
- (3) Sanz, D. N.; Loubeyre, P.; Mezouar, M. *Phys. Rev. Lett.* **2002**, *89*, 245501.
- (4) Vlasse, M.; Naslain, R.; Kasper, J. S.; Ploog, K. J. *Solid State Chem.* **1979**, *28*, 289–301.
- (5) Eremets, M. I.; Struzhkin, V. W.; Mao, H. K.; Hemley, R. J. *Science* **2001**, *293*, 272–274.
- (6) Douglas, B. E.; Ho, S. M. *Structure and Chemistry of Crystalline Solids*; Springer: New York, 2006.
- (7) Masago, A.; Shirai, K.; Katayama-Yoshida, H. *Phys. Rev. B* **2006**, *73*, 104102.
- (8) Van Setten, M. J.; Uijttewaal, M. A.; de Wijs, G. A.; de Groot, R. A. *J. Am. Chem. Soc.* **2007**, *129*, 2458–2465.
- (9) Widom, M.; Mihalkovič, M. *Phys. Rev. B* **2008**, *77*, 064113.
- (10) Qin, J. Q.; Irifune, T.; Dekura, H.; Ohfujii, H.; Nishiyama, N.; Lei, L.; Shinmei, T. *Phys. Rev. B* **2012**, *85*, 014107.
- (11) Solozhenko, V. L.; Kurakevych, O. O. *Sci. Rep.* **2013**, *3*, 2351.
- (12) Zhang, B. *Solid State Commun.* **2014**, *177*, 50–53.
- (13) Oganov, A. R.; Chen, J. H.; Gatti, C.; Ma, Y. Z.; Ma, Y. M.; Glass, C. W.; Liu, Z. X.; Yu, T.; Kurakevych, O. O.; Solozhenko, V. L. *Nature* **2009**, *457*, 863–867.
- (14) Solozhenko, V. L.; Kurakevych, O. O.; Oganov, A. R. *J. Superhard Mater.* **2008**, *30*, 428–429.
- (15) Oganov, A. R.; Solozhenko, V. L. *J. Superhard Mater.* **2009**, *31*, 285–291.
- (16) Qin, J. Q.; Nishiyama, N.; Ohfujii, H.; Shinmei, T.; Lei, L.; He, D. W.; Irifune, T. *Scr. Mater.* **2012**, *67*, 257–260.
- (17) Jiang, C.; Lin, Z. J.; Zhang, J. Z.; Zhao, Y. S. *Appl. Phys. Lett.* **2009**, *94*, 191906.
- (18) Zhou, W.; Sun, H.; Chen, C. F. *Phys. Rev. Lett.* **2010**, *105*, 215503.
- (19) Zhang, B.; Liang, Y. C.; Sun, H. Y. *J. Phys: Condens. Matter* **2007**, *19*, 346224.
- (20) An, Q.; Luo, S. N.; Han, L. B.; Zhng, L. Q.; Tschauner, O. J. *Phys: Condens. Matter* **2008**, *20*, 095220.
- (21) Wang, S. J.; Wang, H.; Du, K.; Zhang, W.; Sui, M. L.; Mao, S. X. *Nat. Commun.* **2014**, *5*, 3433.
- (22) Simha, N. K. *J. Mech. Phys. Solids* **1997**, *45*, 261–292.
- (23) Swain, M. V. *Nature* **1986**, *322*, 234–236.
- (24) Song, Y. T.; et al. *Nature* **2013**, *502*, 85–88.
- (25) Lai, A.; Du, Z. H.; Gan, C. L.; Schuh, C. A. *Science* **2013**, *341*, 1505–1508.
- (26) Christian, J. W. *Physical Properties of Martensite and Bainite*; The Iron and Steel Institute: Scarborough (UK), 1965.
- (27) Christian, J. W. *The Theory and Transformations in Metals and Alloys*; Pergamon Press: Oxford, 1975.
- (28) Walia, H.; Brantley, W. A.; Gerstein, H. J. *Endod.* **1988**, *14*, 346–351.
- (29) Srivastava, V.; Song, Y.; Bhatti, K.; James, R. D. *Adv. Energy Mater.* **2011**, *1*, 97–104.
- (30) Bhattacharya, K. *Microstructure of Martensite: Why It Forms and How It Gives Rise to the Shape-Memory Effect*; Oxford University Press: Oxford, 2003.
- (31) Kresse, G.; Hafner, J. *Phys. Rev. B* **1993**, *47*, 558–561.
- (32) Kresse, G.; Furthmüller, J. *Comput. Mater. Sci.* **1996**, *6*, 15–50.
- (33) Kresse, G.; Furthmüller, J. *Phys. Rev. B* **1996**, *16*, 11169–11186.
- (34) Kresse, G.; Joubert, D. *Phys. Rev. B* **1999**, *59*, 1758–1775.
- (35) Roundy, D.; Krenn, C. R.; Cohen, M. L.; Morris, J. W., Jr. *Phys. Rev. Lett.* **1999**, *82*, 2713–2716.
- (36) Togo, A.; Oba, F.; Tanaka, I. *Phys. Rev. B* **2008**, *78*, 134106.
- (37) Xiao, H.; Tahir-Kheli, J.; Goddard, W. A., III. *J. Phys. Chem. Lett.* **2011**, *2*, 212–217.
- (38) Dovesi, R.; Saunders, V. R.; Roetti, C.; Orlando, R.; Zicovich-Wilson, C. M.; Pascale, F.; Civalieri, B.; Doll, K.; Harrison, N. M.;

Bush, I. J.; et al. *CRYSTAL 2009 User's Manual*; University of Torino: Torino, Italy, 2009.

(39) Peintinger, M. F.; Oliveira, D. V.; Bredow, T. J. *Comput. Chem.* **2013**, *34*, 451–459.

(40) Le Page, Y.; Saxe, P. *Phys. Rev. B* **2002**, *65*, 104104.

(41) Chung, D. H. *Philos. Mag.* **1963**, *8*, 833–841.

(42) Pugh, S. F. *Philos. Mag.* **1954**, *45*, 823–843.

(43) Li, K. Y.; Wang, X. T.; Zhang, F. F.; Dongfeng Xue, D. F. *Phys. Rev. Lett.* **2008**, *100*, 235504.

(44) Lyakhov, A. O.; Oganov, A. R. *Phys. Rev. B* **2011**, *84*, 092103.

(45) Wade, K. J. *Chem. Soc. D* **1971**, *15*, 792–793.

(46) H€aussermann, U.; Mikhaylushkin, S. A. *Inorg. Chem.* **2010**, *49*, 11270–11275.

(47) Becke, A. D.; Edgecombe, K. E. *J. Chem. Phys.* **1990**, *92*, 5397–5403.

(48) Silvi, B.; Savin, A. *Nature (London)* **1994**, *371*, 683–686.

(49) Matkovich, V. I. *J. Am. Chem. Soc.* **1961**, *83* (8), 1804–1806.

(50) He, D.; Zhao, Y.; Daemen, L.; Qian, J.; Shen, T. D.; Zerda, T. *W. Appl. Phys. Lett.* **2002**, *81* (4), 643–645.

(51) Perdew, J. P.; Levy, M. *Phys. Rev. Lett.* **1983**, *51*, 1884–1887.

(52) Sham, L. J.; Schlüter, M. *Phys. Rev. Lett.* **1983**, *51*, 1888–1891.